NANO LETTERS
pubs.acs.org/NanoLett
Letter

Hierarchical Capillarity-Assisted Liquid Invasion in Multilayered Paper Channels for Nanoelectrokinetic Preconcentration

Joowon Seo,[∇] Sohyun Jung,[∇] Jihee Park, Ho-Young Kim,[*] and Sung Jae Kim[*]

Cite This: *Nano Lett.* 2023, 23, 8065–8072

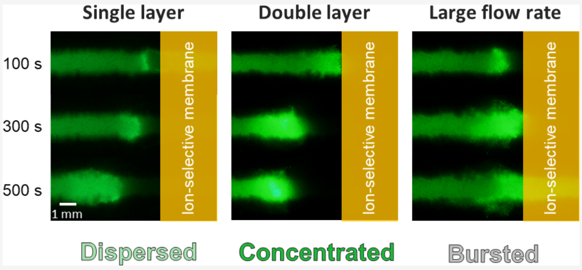

ABSTRACT: A nanoelectrokinetic phenomenon called ion concentration polarization (ICP) has been recently applied to microfluidic paper-based devices for the high fold preconcentration of low-abundant analytes. The inherent microstructural characteristics of cellulose papers can sufficiently stabilize the chaotic electroconvection of ICP, which is a significant annoyance for typical engineered microfluidic channels. However, a high electrical voltage to induce ICP in a paper-fluidic channel can increase unavoidable electrophoretic forces over drag forces so that the preconcentrated plug is rapidly receded with severe dispersion. In order to enhance the hydraulic drag force that helps the preconcentration of analytes, here we introduce a multilayered paper structure into paper-fluidic channel. We theoretically and experimentally demonstrate that a hierarchical capillary structure in a multilayered paper-fluidic channel can effectively increase the hydraulic drag force. For the practical utility in the field of diagnostics, the mechanism is verified by a simple example of the immunoassay using biotin−streptavidin complexation.

KEYWORDS: *nanoelectrokinetics, ion concentration polarization, multilayered paper-fluidic channels, hierarchical capillarity, molecular preconcentration*

Recently, an ion concentration polarization (ICP) phenomenon has often been applied to preconcentrate analytes within microchannels. This trapping method using the ICP phenomenon has the virtue of a high preconcentration factor within a short time interval and is easily integrated with downstream analysis parts.[1,2] This ICP phenomenon in the microchannel is induced in the vicinity of an ion-selective membrane immersed in an electrolyte solution under an external voltage.[3−5] With a cation-selective nanoporous (1−10 nm) membrane such as Nafion,[6] anions moving toward the anode are blocked by the membrane, while cations can freely penetrate the membrane and keep moving in the direction to the cathode. Thus, both ions are depleted on the anodic side of the membrane due to electroneutrality, forming an ion depletion zone (IDZ).[7,8] Concurrently, negatively charged analytes are expelled from this IDZ. When these analytes experience the opposing force by the flow, for example, electrokinetic flow[1,9] or hydraulic pressure-driven flow,[10] the analytes are effectively accumulated outside the virtual barrier of IDZ where electrophoretic force and hydraulic drag force are balanced.[11−14] This circumstance is how the ICP phenomenon operates during the preconcentration of the analytes within the microchannels.

However, the preconcentrated plug could be perturbed by the instability of the convective flow in the IDZ, which is induced as follows. The lack of ions in IDZ significantly reduces the conductivity in the region. Consequently, the electric field is locally amplified to satisfy the electric current continuity, and the extended space charge layer only with cations is extended near the membrane.[15,16] A small heterogeneity of the membrane surface distorts the extended space charge layer, inducing the gradient of ion concentration and subsequent electric body force, which are tangential to the membrane. The resultant tangential motion and the mass conservation of the fluid give rise to a vortical electroconvection (EC) in the IDZ.[16−20] In addition, the vortex becomes chaotic under a strong external voltage to induce the intensive ICP. This chaotic EC is a crucial annoyance in engineering management for microfluidic preconcentration. Therefore, auxiliary microstructures such as dielectric pillars or microfin networks have been introduced into the microchannels to stabilize the EC.[21,22] Under the large area-to-volume ratio of the microstructure, the ion transport mechanism changes from electro-convective instability (EOI) to surface conduction (SC) and electroosmotic flow (EOF), where they are largely categorized as stable conditions.[23] While the additional microstructures successfully guided the direction of the EC and inhibited its chaotic properties, the sophisticated

Received: May 31, 2023
Revised: July 30, 2023
Published: August 15, 2023

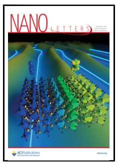

https://doi.org/10.1021/acs.nanolett.3c02044
Nano Lett. 2023, 23, 8065–8072

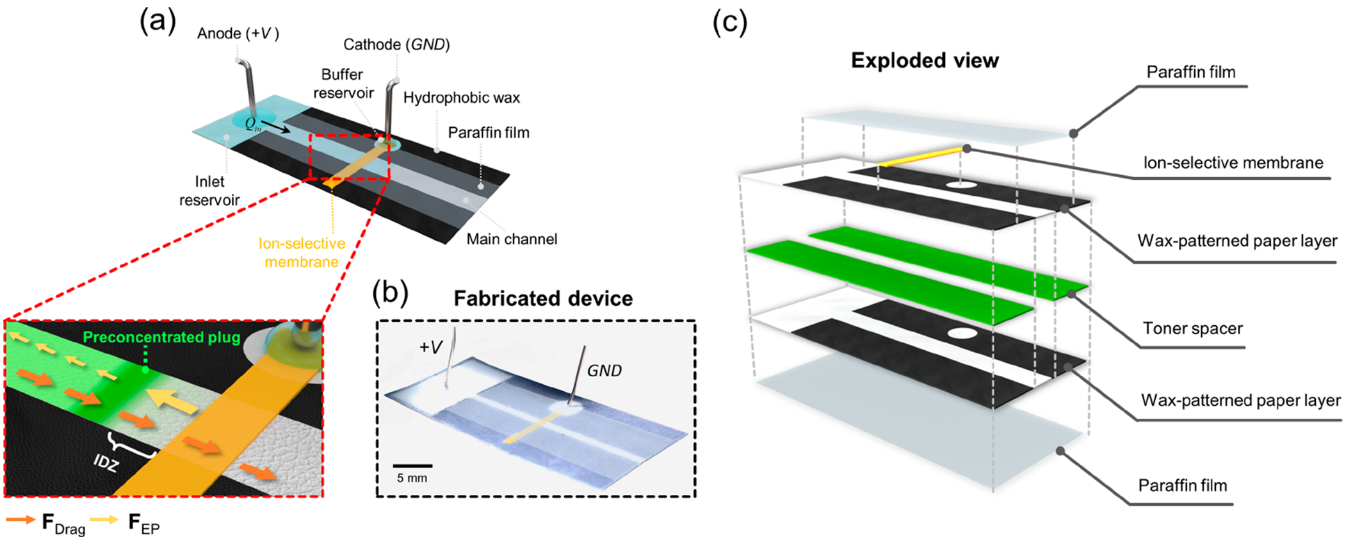

Figure 1. (a) Schematic diagram of paper-fluidic channel as a nanoelectrokinetic preconcentrator. Inset image shows the nanoelectrokinetically preconcentrated plug near the boundary of the ion depletion zone, where the drag force ($\mathbf{F}_{\mathbf{Drag}}$) and the amplified electrophoretic force ($\mathbf{F}_{\mathbf{EP}}$) by the boosted electric field due to the lack of ions near the nanoporous membrane are balanced. (b) Photograph of the fabricated nanoelectrokinetic paper-based device. (c) Exploded schematic of the hierarchical capillarity-assisted nanoelectrokinetic preconcentrator, which is fabricated by stacking multifilms.

fabrication and manipulation within the microchannel are inevitably elaborate and exquisite processes.

Instead of utilizing the finely fabricated microchannel, we here apply a paper-fluidic channels with a cellulose fiber network to detour the manufacturing difficulties and high cost. The inherent microstructural characteristics of cellulose papers enable sufficient stabilization of the EC and the preconcentration plug.[24] Therefore, it is possible to regard the paper as a highly multiplexed fluidic channel and thus provide an adequate sample volume for an image analysis without EC instability. Furthermore, the sample solution is spontaneously absorbed through the paper by capillarity, making the paper-based device free of an external apparatus for pumping and easy to use.

In a paper-fluidic channel where the anode and cathode terminals are located on the inlet and near the ion-selective membrane, as shown in Figure 1, the aforementioned ICP preconcentration mechanism can also be applied. (see Supporting Information (SI) Note 1 for detailed fabrication). The hydrodynamic drag force ($\mathbf{F}_{\mathbf{Drag}}$; orange arrow) propels the analytes toward the ion-selective membrane, and simultaneously, the electrophoretic force exerted by an external electric field ($\mathbf{F}_{\mathbf{EP}}$; yellow arrow) pushes the analytes away from the ion-selective membrane. Particularly, the electrophoretic force near IDZ is amplified by the increased electric field due to the lack of ions in the IDZ. In this circumstance, the amplified electrophoretic force is balanced with drag force in the vicinity of IDZ, where the preconcentrated plug would have shown stacking behavior in our previous study.[25,26] However, the paper-based device needs a higher external voltage to develop sufficient ICP for the preconcentration of the analytes due to its relatively large scale compared with a lithographically fabricated microfluidic channel. With the higher voltage, the electrophoretic force becomes more dominant than the hydrodynamic drag force so that the concentrated plug is broadened and propagates in the inlet direction, inferring a low preconcentration ratio of the analyte. Therefore, it is necessary to enhance the hydrodynamic drag force versus the electrophoretic force.

For capillary-driven flow in porous media, its rate is determined by the pore size, according to Darcy's law. Thus, enhancing the drag force on the analytes in the paper-fluidic channel requires an increment in pore size, but it is limited. Several strategies for accelerating the capillary flow in papers have been developed by simply stacking the paper itself[27] or paper and plastic film.[28] When the papers are stacked, a hierarchical capillary structure composed of the intrinsic pore of the paper layer and the air gap between the paper layers is formed, which increases the liquid imbibition rate compared to a single-layer paper.[27] However, understanding the fundamental physics of fast flow by a hierarchical capillarity in those stacked papers falls short of demands. In this work, we experimentally and theoretically study the dynamics of hierarchical capillarity-assisted liquid invasion in microfluidic multilayer paper-based devices. We then find that the air gap created between the paper layers while stacking them serves as a highway for liquid transport; thereby, the rate of liquid imbibition in the paper-fluidic channel increases. Based on our theoretical model, we propose an optimal number of paper layers for a paper-fluidic channel in terms of operation-effectiveness. We then experimentally show that multilayer paper-based devices have improved performance over single-layer ones by shortening the sample loading time and alleviating the dispersion and propagation of the preconcentration plug. Finally, we verify the enhanced performance with biotin−streptavidin complexation as a simple example of an immunoassay.

To investigate the liquid imbibition dynamics in microfluidic multilayer paper-based devices, we first fabricate paper channels with different numbers of layers, ranging from single to quadruple, and observe the propagation of phosphate-buffered saline (PBS) through them. Figure 1c only shows double-layer device. One can fabricate multilayer device by repeating the stacking of toner spacer and wax-patterned paper layer. Comparing the temporal evolution of liquid imbibition

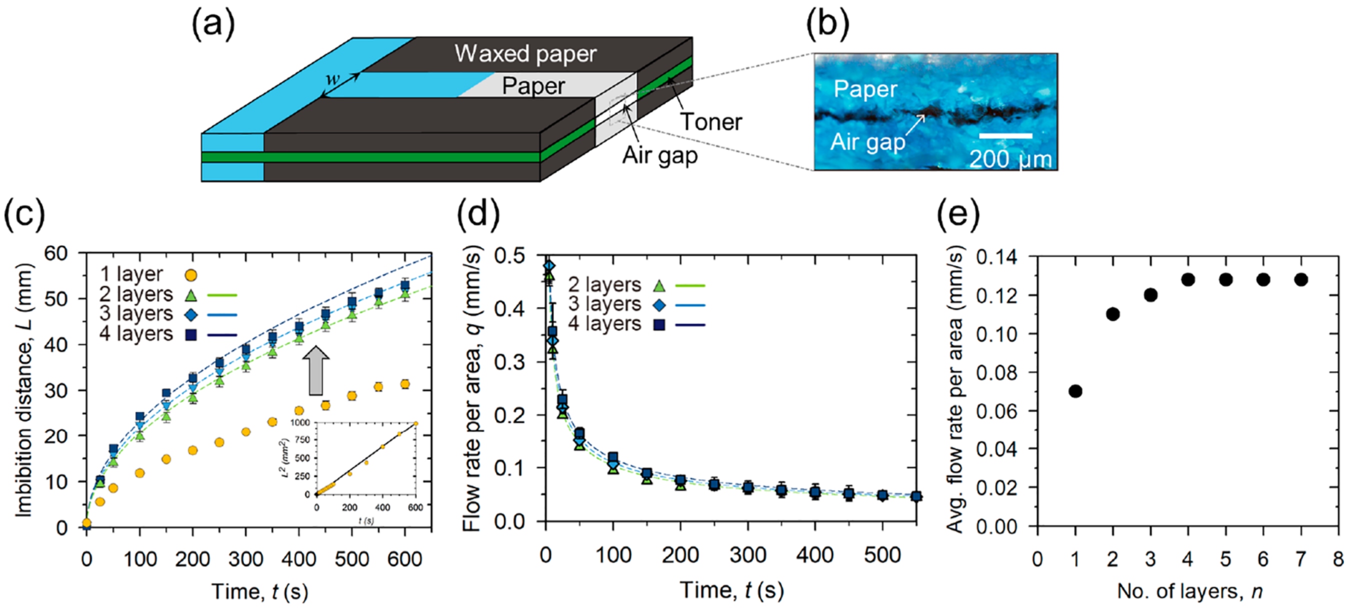

Figure 2. (a) Schematic illustrations of a multilayer paper channel consisting of several paper layers aligned and adhered together in nonchannel parts that are waxed papers with a toner. (b) Microscopy image of small air gaps created between the paper layer, measuring 10 μm in height h. (c) Liquid imbibition distance, L, versus time, t, in multilayer paper channels with a different number of layers n, such as $n = 1$ (yellow circle), $n = 2$ (green triangle), $n = 3$ (blue diamond), and $n = 4$ (navy square). The dotted colored lines show the theoretical imbibition distance in each multilayer paper channel calculated according to eq 1. Inset: Square of the liquid imbibition distance versus time in a single-layer paper channel. The solid black line is the best-fitting line with a slope corresponding to $D_P{}^2$ and a value of 2.7×10^{-12} m^2/s^2. (d) Liquid flow rate per unit area, Q, versus time in multilayer paper channels with different layers, from double to quadruple. The dotted colored lines represent the theoretical flow rate per unit area in each multilayer paper channel calculated by eq S5. (e) The theoretical average flow rate per unit area between 1 and 600 s in n-layer paper channels in $1 \leq n \leq 7$.

distances, L, reveals that experimentally measured L increases on average by 70% in the double-layer channel than in the single-layer channel. L increases on average by 8% in the triple-layer than in the double-layer and 5% in the quadruple-layer than in the triple-layer.

To understand the observed increase in liquid flow rate in multilayered channels, we theoretically analyzed the liquid behavior in these channels, considering the distinctive structural characteristics of these channels. As explained in SI Note 2, we find that capillarity is the more prominent driving mechanism in centimetric paper-fluidic channels under high-intensity electric fields because it drives flow at a rate 10^3 times greater than that of electroosmotic flow. The multilayer paper channels exhibit a hierarchical pore structure, owing to the presence of thin air gaps formed between the paper layers because the paper layers, which are aligned and stacked, are glued to each other in nonchannel parts corresponding to waxed papers with a toner of thickness h (see Figure 2b). As the thin air gaps correspond to pores larger than those within the paper itself, they serve as major conduits for liquid flow. Thus, rapid imbibition occurs through these gaps while concurrently filling the paper pores by flowing outward from the gaps. Taking into consideration this hierarchical capillarity effect, we construct a theoretical model for liquid imbibition in multilayer paper channels. As delineated in the Supporting Information, the imbibition length in the multilayered paper is given by the following:

$$L_n = \sqrt{\frac{\sigma h^2}{3\mu(h+\eta)}t} \qquad (\eta = d\ln(2^{(2-\bar{n})/2}d/\delta^*)) \tag{1}$$

where σ is the surface tension, μ is the viscosity, d is the thickness of paper, δ^* is an infinitesimal liquid imbibition distance in the paper layer, n is the number of paper layers in multilayer paper channels, and $\bar{n} = n$ for $n = 2$, 3, or 4 for $n \geq 4$.

We now calculate the theoretical liquid imbibition distance and its flow rate per unit area using eq 1 for the double- to quadruple-layer paper channels. The calculation results are plotted as colored dashed lines in Figure 2c,d. Here, we use $\delta^* = 10$ μm, which is a reasonable value for filter paper with a mesh size of 11 μm. We see that the calculated imbibition distance and the flow rate per unit area are consistent with the experimental data in those multilayer paper channels.

In addition, we theoretically calculated the average flow rate per unit area in n-layer paper channels for $1 \leq n \leq 7$ and plotted the results in Figure 2e. The flow rate in the double-layer paper channel is 60% higher than single-layer paper channel, but the flow rate in the multiple paper channels with more than two layers increases by less than 7% with the addition of layers. As adding paper layers is a significantly labor-intensive process, we conclude that the double-layer paper channel is the most cost-effective design for enhancing the hydraulic drag force on analytes in a paper-fluidic channel.

Now, we demonstrate how the increased flow rate affects the balance of electrophoretic force and drag force and the consequent preconcentration behavior in the paper-fluidic channel. We fabricated preconcentration devices by attaching an ion-selective membrane to the paper devices, which were theoretically analyzed in Figure 2 (see SI Note 1 for detailed fabrication). Figure 3 compares the results of the preconcentration experiments with (a) a single-layer device, (b) a double-layer device, and (c) a single-layer device with larger pores for a significantly stronger drag force. For the preconcentration experiments, we loaded a PBS-based electrolyte solution with fluorescent dyes into the inlet and buffer

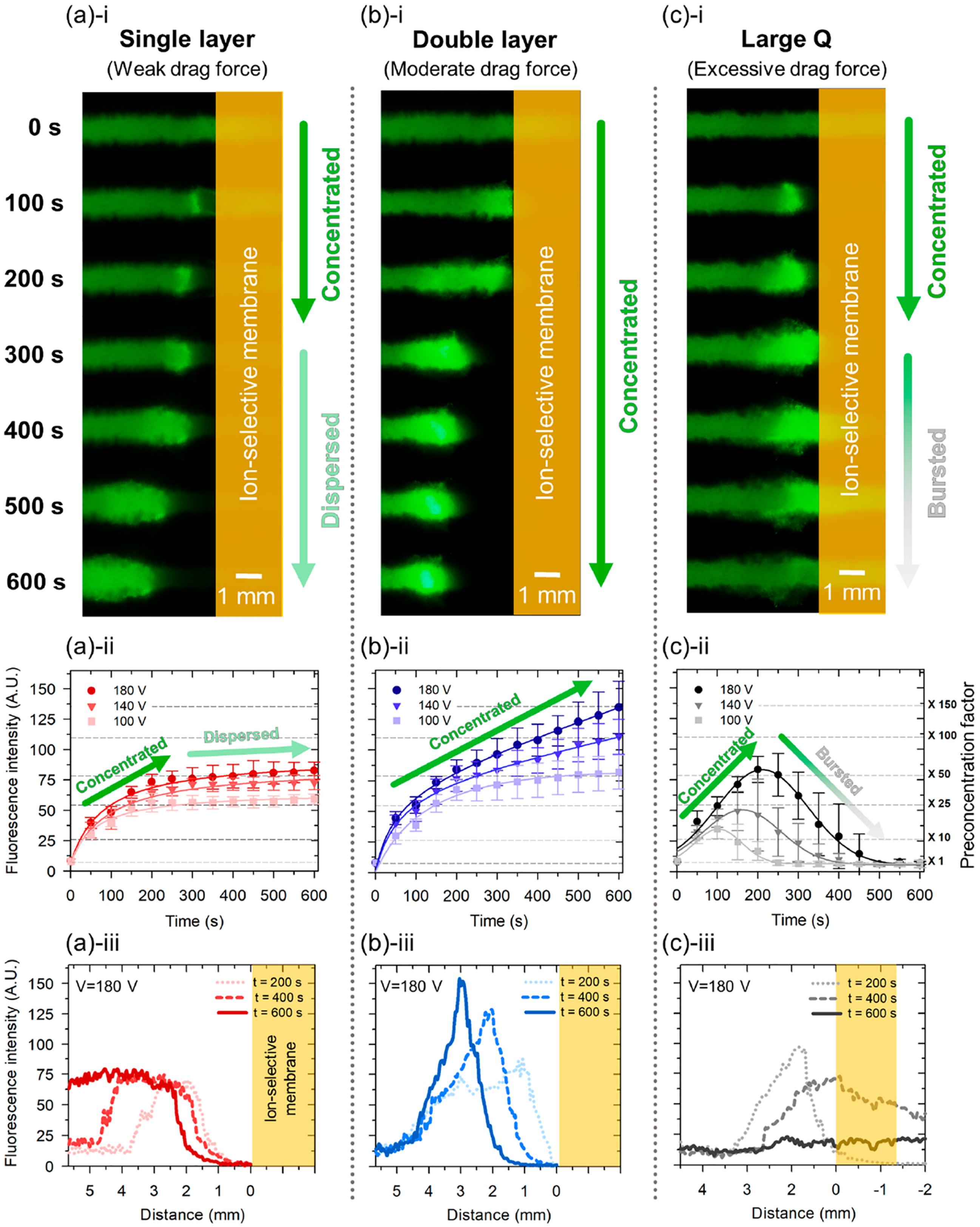

Figure 3. Experimental results of nanoelectrokinetic preconcentration depending on drag forces in (a) a single-layer device, (b) a double-layer device, and (c) a single-layer device with larger pores for significantly stronger drag force. For each column of a−c, the first row (i) shows a time series snapshot of the preconcentration process for 10 min. In the second row (ii), averaged fluorescence intensity over time is measured from captured snapshots. 100 V, 140 V, and 180 V are chosen for operational voltage. The third row (iii) presents the fluorescence intensity plots as line profiles starting from the surface of the ion-selective membrane during the preconcentration process.

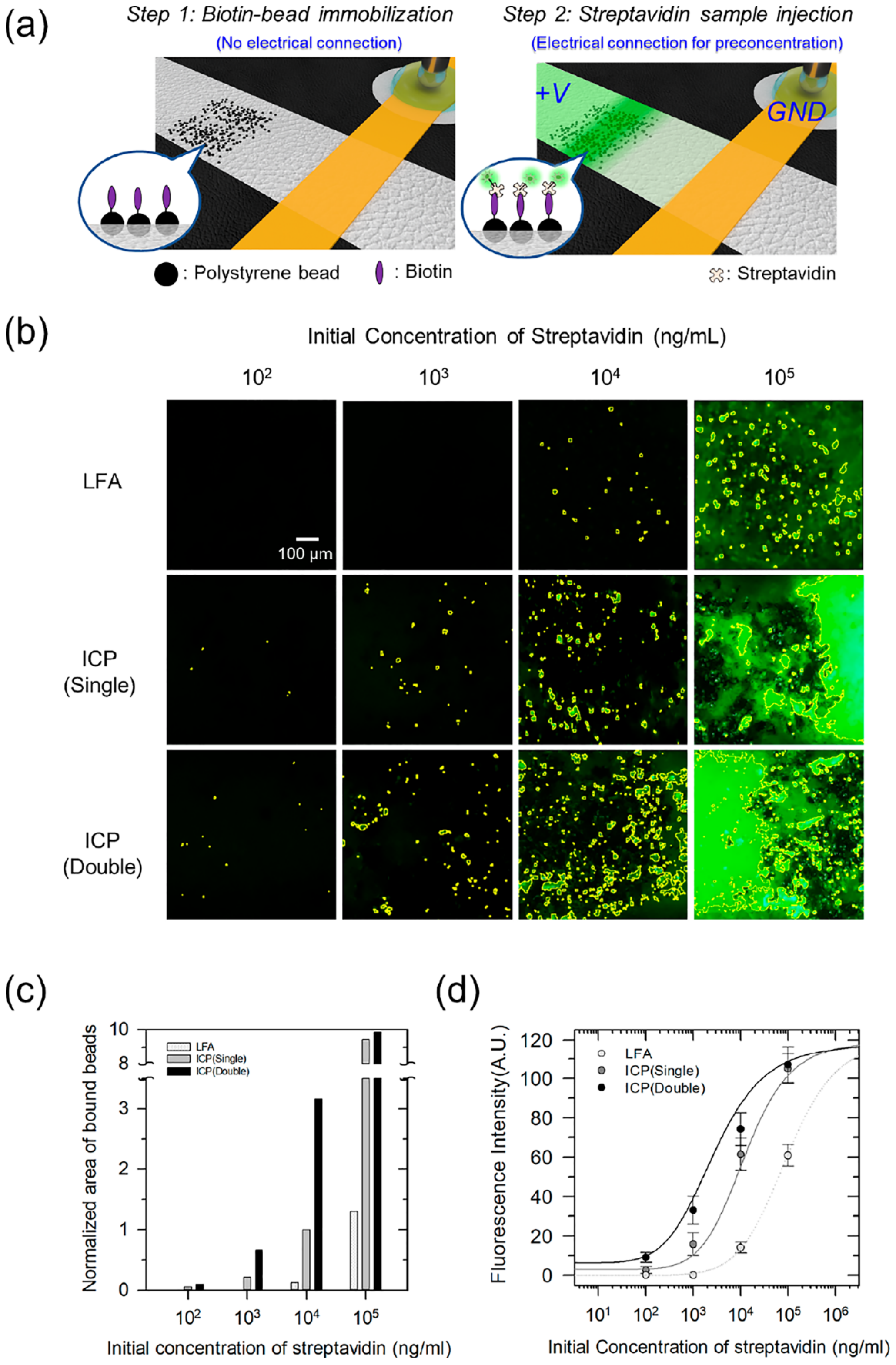

Figure 4. Demonstration of bead-based immunofluorescence assay with the hierarchical capillarity-assisted nanoelectrokinetic preconcentration. (a) Schematic diagram of immobilizing biotinylated beads (step 1) and nanoelectrokinetic preconcentration of streptavidin labeled by fluorescent dye (step 2). (b) Fluorescence microscopic images of the bead-imbedded site in the lateral flow assay (LFA), single- and double-layer devices after preconcentration process (ICP). The yellow bounded regions represent a binding signal from biotin−streptavidin complex. (c) The normalized area of beads brightened by the biotin−streptavidin complexation. After preconcentration, the normalized area of brightened beads expands by 300% in the double-layer ICP device compared to in the single-layer ICP device except for the excess streptavidin concentration of 10^5 ng/mL. (d) Binding curves are fitted by immunoassay data at the initial streptavidin concentrations of 10^2 ng/mL, 10^3 ng/mL, 10^4 ng/mL, and 10^5 ng/mL.

reservoir, as shown in Figure 1. When the solution sufficiently wets the ion-selective membrane, an electric voltage is applied (t = 0) at the inlet and the buffer reservoir is grounded. The applied voltage in the paper-fluidic channel is relatively higher

Table 1. *t*-Test of Immunoassay in Single- and Double-Layer Devices[a]

	single			double			*t* test	
streptavidin concentration (ng/mL)	*N*	mean	std. deviation	*N*	mean	std. deviation	*t*	sig. (2-tailed)
10^2	6	2.48	1.58	6	8.54	2.15	−5.06	0.0006
10^3	6	15.68	5.27	6	33.01	6.46	−4.64	0.0009
10^4	6	61.36	7.46	6	74.14	7.63	−2.67	0.0232
10^5	6	104.93	6.88	6	107.02	8.46	−4.64	0.6780 (>0.05)

[a] 95% confidence interval of the difference.

than that in conventional microchannel-based devices because the paper-based device needs to transport more ions for sufficient expansion of the IDZ due to its larger dimensions than the microchannel device[29−32] (see SI Note 3).

The fluorescence images in Figure 3a−i represent the preconcentration process over time at 180 V. The fluorescent analytes seem to be well-preconcentrated for 300 s. However, the preconcentrated plug starts to be receded toward the inlet reservoir and to disperse its compactness. In Figure 3a−ii, the averaged fluorescence intensity of the preconcentrated plug for various operational voltages is measured from the experimental images (see SI Note 3 for detailed image analysis). The fluorescence intensity increases until 300 s and then is saturated afterward, as expected from the plug shapes of Figure 3a−i. Applying a higher voltage in single-layer devices does not change the fluorescence intensity profile (*i.e.*, initially concentrated and then saturated) but slightly increases the preconcentration factor, as shown in Figure 3a−ii. The line profile of fluorescence intensity along the distance from the ion-selective membrane in Figure 3a−iii shows that its plateau not only becomes higher but also only widened despite the continuous inflow of the sample solution over time. Such dispersion of the preconcentration plug indicates that the hydraulic drag force acting oppositely of the electrophoretic force in the single-layer device is not enough to prevent the dispersion of the analytes.

In order to suppress the plug dispersion and consequently facilitate efficient preconcentration, we increase the hydraulic drag force with hierarchical capillarity by adopting multilayer structures. According to the theoretical analysis, the flow rate of a double-layer device increases by 60%. The electrophoretic force is not affected by multilayering because the force is determined only by the electrophoretic mobility of the analytes. However, the drag force can be enhanced in a double-layer device because it is mainly determined by the flow rate. The fluorescence plug brightened for 600 s, as shown in Figure 3b−i. This indicates that the enhanced flow rate can prevent the dispersion of the plug since the capillarity-assisted flow can not only provide more analytes per unit of time but also push the analytes in the opposite direction of the electrophoretic force. As shown in Figure 3b−ii, the fluorescence intensity (*y*-axis on the left) keeps increasing over time, and the preconcentration factor (*y*-axis on the right) reaches 150-fold at 600 s with 180 V. This preconcentration factor is 3 times higher compared to that of the single-layer device under the same conditions. In Figure 3b−iii, the line profile of the fluorescence intensity shows a sharp peak at the balanced position of the electrophoretic and drag forces, while the line profile of the single-layer device remains only as a plateau in Figure 3a−iii.

Figure 3c shows the preconcentration behavior of another single-layer device of larger pore size (∼25 um), inducing excessive drag force relative to any of the original multilayered papers (pore size ∼10 um). The reason for using paper with larger pores is to show preconcentration behavior when the optimum flow rate is exceeded (see SI Note 3 for the imbibition length of the devices). Figure 3c−i shows that the preconcentration plug is initially unstable (see Supporting Video for clear instability) and eventually bursts over the ion-selective membrane. Here, the hydrodynamic drag force by excessive flow rate overcomes not only the electrophoretic force but also the electrostatic repulsion inside IDZ[33] (see the diagram in SI Note 4). In Figure 3c−ii, the fluorescence intensity of the plug increases until 200 s at 180 V but eventually decreases after the plug burst. Also, we can observe that the preconcentrated plug bursts more quickly as the applied voltage decreases. Additionally, once the excessive drag force destroys the IDZ, it cannot be restored under the same voltage conditions so that the preconcentration of the target cannot appear again (Figure 3c−iii). These results show that the excessive drag force destroying the IDZ inhibits the preconcentration efficiency of the paper-fluidic channel.

We now verify the effect of hierarchical capillarity on nanoelectrokinetic preconcentration using a bead-based immunofluorescence assay. The high-affinity streptavidin−biotin complex is utilized to confirm the immunoassay. One simple way of integrating a bead-based immunoassay into a nanofluidic preconcentration device is trapping the microbeads into a micropillar array structure in the microchannel.[34] In this work, the intrinsic porous structure of the cellulose paper can serve to trap the beads without any additional fabrication steps. We immobilized biotinylated beads at the expected preconcentration site in the main channel of the paper-based device, as shown in Figure 4a (step 1). The streptavidin labeled by the fluorescent dye in 1× PBS solution is loaded at the inlet reservoir and preconcentrated by ICP (step 2). The non-labeled beads would have a fluorescence signal once the dye binds to the beads so that the nanoelectrokinetic preconcentration process can enhance not only the number of bright beads but also the brightness. The temperature range of the sample solution was measured using a thermochromic pigment, which indicated that the immunoassay reaction could take place without denaturation (see SI Note 3).[35] Also, pH could be significantly changed near the ICP layer due to either electrode reaction[36,37] or ion exchange,[38] but the changes are inconsequential in this work due to larger dimensions and relatively fast capillary flow.

The fluorescence signal of the biotin−streptavidin complex in the bead-imbedded site can be enhanced by the preconcentration owing to the ICP, as shown in Figure 4b. The biotin−streptavidin complex clusters are highlighted with yellow boundary lines, which denote the top 20% of brightness, to analyze the fluorescent intensity from the images. To validate the impact of preconcentration, we conducted a supplementary lateral flow assay (LFA), which relies only on the capillary flow of paper without electrical stimulation (see the diagram in SI Note 4). The stronger fluorescence signals indicate that more reaction would be activated. In this way, we can count the total number of pixels bound by a yellow line, which indicates the bound beads. Figure 4c shows the normalized area of beads brightened by the biotin−streptavidin complexation as a function of the initial streptavidin concentrations. As indicated, the area significantly increases by ICP preconcentration and optimization of the device. Furthermore, binding curves can be obtained, as shown in Figure 4d. The *t*-test is conducted to confirm that the fluorescent signals of single- and double-layer ICP devices are distinguishable at 10^2 ng/mL, 10^3 ng/mL, and 10^4 ng/mL (Table 1). Note that the images are largely overwhelmed by background fluorescent dye at 10^5 ng/mL, so we regard this condition as perfect binding. For standard curve fitting of immunoassay data, four-parameter logistic regression ($y = d + (a - d)/(1 + (x/c)^b)$) is employed, where a and d are the theoretical response at zero and infinite concentrations, respectively, b is the slope factor, and c is the midrange concentration.[39] These parameters are calculated using commercial software (Sigma Plot, SPSS Inc.), providing a correlation coefficient (R^2) larger than 0.99. Then, we can calculate the limit of detection (LOD), which is defined as the concentration value when the fluorescence intensity is as high as 3 times the standard deviation of the fitted curve from the zero-dose response. The measured LODs are 3691.5, 634.7, and 118.1 ng/mL for LFA and ICP (single)- and ICP (double)-layer devices, respectively. This result demonstrates that the single-layer ICP device has a 6-fold enhancement in sensitivity attributed to the ICP preconcentration compared to LFA. Moreover, by using a double-layer ICP device, a 5-fold performance improvement is achieved compared to using the single-layer ICP device. Therefore, the ICP preconcentration and the increased drag force by paper staking produce an overall enhancement of 30-fold based on the LOD values.

Detection of low-abundant analytes without sophisticated detectors has been a critical challenge in various fields. In this work, first, we have experimentally and theoretically studied the dynamics of hierarchical capillarity-assisted liquid invasion in a multilayered paper-fluidic channel (Figure 2) and then demonstrated that the preconcentration of analytes in a paper-fluidic channel is enhanced by the hierarchical capillarity (Figure 3). The key idea of these studies is based on the fact that the hierarchical capillary structure composed of intrinsic paper pores and the air gap between paper layers increases the hydraulic drag force in the multilayered paper-fluidic channel. The increased drag force by multilayering shortens the sample loading time and alleviates the dispersion and propagation of the preconcentration plug in the multilayered paper-fluidic channel so that the preconcentration performance is significantly improved compared to that of single-layer ones. However, our study reveals that the effect of one additional paper layer on the increase of the hydraulic drag force has faded in multiple paper channels with three or more paper layers (Figure 2e), and the excessive drag force induced by the larger pore of paper has rather inhibited the preconcentration efficiency in the paper-fluidic channel (Figure 3c). Therefore, we propose that the double-layered paper device is an optimal design for improving the preconcentration of analytes in the paper-fluidic channel in terms of operational effectiveness. Moreover, the effect of multilayering on the preconcentration of analytes is successfully demonstrated in a simple example of immunoassay with biotin−streptavidin complexation, which clearly shows the applicability of this multilayered paper-fluidic channel in the real-world diagnosis area.

■ ASSOCIATED CONTENT

Supporting Information

The Supporting Information is available free of charge at https://pubs.acs.org/doi/10.1021/acs.nanolett.3c02044.

Note 1, methods; Note 2, theoretical modeling; Note 3, additional experiments; Note 4, additional diagrams (PDF)

Experimental results for hierarchical capillarity-assisted nanoelectrokinetic preoconcentration (MP4)

■ AUTHOR INFORMATION

Corresponding Authors

Ho-Young Kim − *Department of Mechanical Engineering, SOFT Foundry Institute, and Institute of Advanced Machines and Design, Seoul National University, Seoul 08826, Republic of Korea*; Email: hyk@snu.ac.kr

Sung Jae Kim − *Department of Electrical and Computer Engineering, SOFT Foundry Institute, and Inter-university Semiconductor Research Center, Seoul National University, Seoul 08826, Republic of Korea*; orcid.org/0000-0002-8622-1765; Email: gates@snu.ac.kr

Authors

Joowon Seo − *Department of Electrical and Computer Engineering, Seoul National University, Seoul 08826, Republic of Korea*; orcid.org/0000-0002-8282-7129

Sohyun Jung − *Department of Mechanical Engineering, Seoul National University, Seoul 08826, Republic of Korea*

Jihee Park − *Department of Electrical and Computer Engineering, Seoul National University, Seoul 08826, Republic of Korea*

Complete contact information is available at: https://pubs.acs.org/10.1021/acs.nanolett.3c02044

Author Contributions

$^\nabla$These authors contributed equally.

Author Contributions

J.S.: methodology, experimental investigation, writing—review and editing. S.J.: methodology, theoretical investigation, writing—review and editing. J.P.: writing—review and editing. H.-Y.K.: theoretical investigation, resources, writing—original draft, supervision, funding acquisition. S.J.K.: resources, writing—original draft, writing—review and editing, supervision, funding acquisition

Notes

The authors declare no competing financial interest.

■ ACKNOWLEDGMENTS

S.J.K., J. S. and J. P. were supported by the Ministry of Science and ICT, South Korea (#NRF-2021R1A4A2001553 and #NRF-2020R1A2C3006162) and the Ministry of Health and Welfare (#HI22C0472000022). H.-Y. K. and S. J. were supported by the Ministry of Science and ICT, South Korea (#NRF-2018R1A3B1052541 and #NRF-2021M3F7A1017476). S. J. was partially supported by #NRF-2022R1I1A1A01066046. Also, all authors acknowledged the support from BK21 FOUR program at Seoul National University.

REFERENCES

(1) Kim, S. J.; Song, Y.-A.; Han, J. Nanofluidic concentration device for biomolecules utilizing ion concentration polarization: theory, fabrication, and applications. *Chem. Soc. Rev.* **2010**, *39* (3), 912−922.

(2) Shen, M.; Yang, H.; Sivagnanam, V.; Gijs, M. Microfluidic protein preconcentrator using a microchannel-integrated nafion strip: Experiment and modeling. *Analytical chemistry* **2010**, *82* (24), 9989−9997.

(3) Schoch, R. B.; Han, J.; Renaud, P. Transport phenomena in nanofluidics. *Reviews of modern physics* **2008**, *80* (3), 839.

(4) Mani, A.; Zangle, T. A.; Santiago, J. G. On the propagation of concentration polarization from microchannel− nanochannel interfaces Part I: analytical model and characteristic analysis. *Langmuir* **2009**, *25* (6), 3898−3908.

(5) de Valença, J. C.; Wagterveld, R. M.; Lammertink, R. G.; Tsai, P. A. Dynamics of microvortices induced by ion concentration polarization. *Phys. Rev. E* **2015**, *92* (3), 031003.

(6) Mauritz, K. A.; Moore, R. B. State of understanding of Nafion. *Chem. Rev.* **2004**, *104* (10), 4535−4586.

(7) Nam, S.; Cho, I.; Heo, J.; Lim, G.; Bazant, M. Z.; Moon, D. J.; Sung, G. Y.; Kim, S. J. Experimental verification of overlimiting current by surface conduction and electro-osmotic flow in microchannels. *Phys. Rev. Lett.* **2015**, *114*, 114501.

(8) Kwon, S.; Lee, H.; Kim, S. J. Pulsed electric field-assisted overlimiting current enhancement through a perm-selective membrane. *Lab Chip* **2021**, *21*, 2153−2162.

(9) Yuan, X.; Renaud, L.; Audry, M.-C.; Kleimann, P. Electrokinetic biomolecule preconcentration using xurography-based micro-nano-micro fluidic devices. *Analytical chemistry* **2015**, *87* (17), 8695−8701.

(10) Marczak, S.; Richards, K.; Ramshani, Z.; Smith, E.; Senapati, S.; Hill, R.; Go, D. B.; Chang, H. C. Simultaneous isolation and preconcentration of exosomes by ion concentration polarization. *Electrophoresis* **2018**, *39* (15), 2029−2038.

(11) Plecis, A.; Nanteuil, C.; Haghiri-Gosnet, A.-M.; Chen, Y. Electropreconcentration with charge-selective nanochannels. *Analytical chemistry* **2008**, *80* (24), 9542−9550.

(12) Cheow, L. F.; Sarkar, A.; Kolitz, S.; Lauffenburger, D.; Han, J. Detecting kinase activities from single cell lysate using concentration-enhanced mobility shift assay. *Analytical chemistry* **2014**, *86* (15), 7455−7462.

(13) Choi, J.; Huh, K.; Moon, D. J.; Lee, H.; Son, S. Y.; Kim, K.; Kim, H. C.; Chae, J.-H.; Sung, G. Y.; Kim, H.-Y.; Hong, J. W.; Kim, S. J. Selective preconcentration and online collection of charged molecules using ion concentration polarization. *RSC Adv.* **2015**, *5* (81), 66178−66184.

(14) Ma, B.; Song, Y.-Z.; Niu, J.-C.; Wu, Z.-Y. Highly efficient sample stacking by enhanced field amplification on a simple paper device. *Lab Chip* **2016**, *16* (18), 3460−3465.

(15) Dukhin, S. S. Electrokinetic phenomena of the second kind and their applications. *Advances in colloid and interface science* **1991**, *35*, 173−196.

(16) Rubinstein, I.; Zaltzman, B. Electro-osmotically induced convection at a permselective membrane. *Phys. Rev. E* **2000**, *62* (2), 2238.

(17) Rubinstein, I.; Maletzki, F. Electroconvection at an electrically inhomogeneous permselective membrane surface. *Journal of the Chemical Society, Faraday Transactions* **1991**, *87* (13), 2079−2087.

(18) Rubinstein, S. M.; Manukyan, G.; Staicu, A.; Rubinstein, I.; Zaltzman, B.; Lammertink, R. G.; Mugele, F.; Wessling, M. Direct observation of a nonequilibrium electro-osmotic instability. *Physical review letters* **2008**, *101* (23), 236101.

(19) Lee, D.; Choi, D.; Park, H.; Lee, H.; Kim, S. J. Electroconvective circulating flows by asymmetric Coulombic force distribution in multiscale porous membrane. *J. Membr. Sci.* **2021**, *636*, 119286.

(20) Seo, M.; Kim, W.; Lee, H.; Kim, S. J. Non-negligible effects of reinforcing structures inside ion exchange membrane on stabilization of electroconvective vortices. *Desalination* **2022**, *538*, 115902.

(21) Lee, H.; Sohn, S.; Alizadeh, S.; Kwon, S.; Kim, T. J.; Park, S.-M.; Soh, H. S.; Mani, A.; Kim, S. J. Overlimiting current in non-uniform arrays of microchannels: recirculating flow and anticrystallization. *Nano Lett.* **2021**, *21*, 5438−5446.

(22) Huh, K.; Yang, S.-Y.; Park, J. S.; Lee, J. A.; Lee, H.; Kim, S. J. Surface conduction and electroosmotic flow around charged dielectric pillar arrays in microchannels. *Lab Chip* **2020**, *20* (3), 675−686.

(23) Sohn, S.; Cho, I.; Kwon, S.; Lee, H.; Kim, S. J. Surface conduction in a microchannel. *Langmuir* **2018**, *34*, 7916−7921.

(24) Baek, S.; Choi, J.; Son, S. Y.; Kim, J.; Hong, S.; Kim, H. C.; Chae, J.-H.; Lee, H.; Kim, S. J. Dynamics of driftless preconcentration using ion concentration polarization leveraged by convection and diffusion. *Lab Chip* **2019**, *19* (19), 3190−3199.

(25) Lee, S.; Hong, S.; Park, J.; Koh, Y.; Lee, H.; Yang, J.; Seo, S. W.; Kim, S. J. dCas9-mediated PCR-free detection of oncogenic mutation by non-equilibrium nanoelectrokinetic selective preconcentration. *Anal. Chem.* **2023**, *95*, 5045−5052.

(26) Choi, J.; Baek, S.; Kim, H. C.; Chae, J.-H.; Koh, Y.; Seo, S. W.; Lee, H.; Kim, S. J. Nanoelectrokinetic selective preconcentration based on ion concentration polarization. *BioChip Journal* **2020**, *14*, 100−109.

(27) Camplisson, C. K.; Schilling, K. M.; Pedrotti, W. L.; Stone, H. A.; Martinez, A. W. Two-ply channels for faster wicking in paper-based microfluidic devices. *Lab Chip* **2015**, *15* (23), 4461−4466.

(28) Jahanshahi-Anbuhi, S.; Chavan, P.; Sicard, C.; Leung, V.; Hossain, S. Z.; Pelton, R.; Brennan, J. D.; Filipe, C. D. Creating fast flow channels in paper fluidic devices to control timing of sequential reactions. *Lab Chip* **2012**, *12* (23), 5079−5085.

(29) Han, S. I.; Hwang, K. S.; Kwak, R.; Lee, J. H. Microfluidic paper-based biomolecule preconcentrator based on ion concentration polarization. *Lab Chip* **2016**, *16* (12), 2219−2227.

(30) Li, X.; Luo, L.; Crooks, R. M. Faradaic ion concentration polarization on a paper fluidic platform. *Analytical chemistry* **2017**, *89* (7), 4294−4300.

(31) Gao, H.; Xie, M.-R.; Liu, J.-J.; Fang, F.; Wu, Z.-Y. Electrokinetic stacking on paper-based analytical device by ion concentration polarization with ion exchange membrane interface. *Microfluid. Nanofluid.* **2018**, *22*, 1−8.

(32) Kim, W.; Park, J. S.; Lee, D.; Seo, J.; Lee, L. P.; Kim, S. J. Rapid and accurate nanoelectrokinetic diagnosis of drug-resistant bacteria. *Biosens. Bioelectron.* **2022**, *213*, 114350.

(33) Choi, J.; Mani, A.; Lee, H.; Kim, S. J. Investigation on the stability of random vortices in an ion concentration polarization layer with imposed normal fluid flow. *Micromachines* **2020**, *11*, 529.

(34) Ko, S. H.; Kim, S. J.; Cheow, L. F.; Li, L. D.; Kang, K. H.; Han, J. Massively parallel concentration device for multiplexed immunoassays. *Lab Chip* **2011**, *11* (7), 1351−1358.

(35) Grandke, J.; Resch-Genger, U.; Bremser, W.; Garbe, L.-A.; Schneider, R. J. Quality assurance in immunoassay performance-temperature effects. *Analytical methods* **2012**, *4* (4), 901−905.

(36) Kim, W.; Oh, J.; Kwon, S.; Kim, K.; Kim, S. J. Quantifying the pH shift induced by selective anodic electrochemical reactions in the ion concentration polarization phenomenon. *Lab Chip* **2019**, *19* (8), 1359−1369.

(37) Park, J. S.; Oh, J.; Kim, S. J. Controllable pH manipulations in micro/nanofluidic device using nanoscale electrokinetics. *Micromachines* **2020**, *11* (4), 400.

(38) Seo, M.; Park, S.; Lee, D.; Lee, H.; Kim, S. J. Continuous and spontaneous nanoparticle separation by diffusiophoresis. *Lab Chip* **2020**, *20*, 4118−4127.

(39) Hecht, A. H.; Sommer, G. J.; Durland, R. H.; Yang, X.; Singh, A. K.; Hatch, A. V. Aptamers as affinity reagents in an integrated electrophoretic lab-on-a-chip platform. *Analytical Chemistry* **2010**, *82* (21), 8813−8820.